Changes in Arctic moisture transport over the North Pacific associated with sea ice loss

Marie C. McGraw[1,2] · **Cory F. Baggett[1,3]** · **Chengji Liu[1]** · **Bryan D. Mundhenk[1,4]**

Abstract

Recent work has emphasized the important role of midlatitude moisture fluxes in enhancing Arctic warming and sea ice loss. Conversely, less attention has been paid to the impact of Arctic warming and sea ice loss on midlatitude moisture fluxes. Analysis of an atmosphere-only general circulation model indicates that sea ice loss promotes changes in the large-scale midlatitude atmospheric circulation that have a substantial impact on moisture transport into and out of the Arctic. While poleward moisture transport into the Arctic does increase in a reduced sea ice climate, the increase in equatorward moisture transport out of the Arctic is larger, particularly in boreal winter over the North Pacific. A decomposition of the meridional moisture transport reveals that this increase in equatorward moisture transport is driven, at least in part, by changes in the background circulation. Specifically, sea ice loss drives a series of large-scale tropospheric circulation changes, including an increase in cyclonic Rossby wave breaking over the North Pacific that results in a preferential enhancement of equatorward moisture transport out of the Arctic in the days following the peak of the Rossby wave breaking event.

Keywords Moisture transport · Arctic amplification · Sea ice loss · Rossby wave breaking

1 Introduction

Arctic temperatures have increased substantially faster than the global mean surface temperature in recent decades, a phenomenon known as Arctic amplification (e.g., Serreze and Barry 2011; Cohen et al. 2014; Walsh 2014). Climate model projections indicate that Arctic amplification will continue as global temperatures rise (e.g., Manabe and Stouffer 1980; Hansen et al. 1984; Holland and Bitz 2003; Collins et al. 2013). This warmer Arctic is accompanied by sea ice loss, and thus, further warming due to an increase in absorbed solar radiation, increased heat exchange between the ocean and the atmosphere, and other processes (e.g.,

Manabe and Wetherald 1975; Deser et al. 2010; Serreze and Barry 2011; Serreze et al. 2012; Kapsch et al. 2016; Burt et al. 2016).

Atmospheric water vapor can also substantially impact Arctic temperatures. The water vapor feedback is described by the Clausius–Clapeyron relationship—as temperatures increase, the atmosphere is capable of holding more water vapor (e.g., Held and Soden 2006). Because atmospheric water vapor is a highly effective greenhouse gas, it can trap outgoing longwave radiation and re-emit that radiation downward, leading to surface warming (e.g., Francis and Hunter 2006; Burt et al. 2016). Even small increases in atmospheric water vapor could have a large impact on Arctic climate through a positive feedback loop where surface warming induces sea ice loss and a subsequent enhancement of latent heat fluxes (and thus, atmospheric water vapor) from the ocean to the atmosphere, ultimately leading to further warming (e.g., Screen and Simmonds 2010; Ghatak and Miller 2013; Burt et al. 2016).

Increased atmospheric water vapor in the Arctic has been linked to moist intrusions from lower latitudes. These intrusions lead to a reduction in sea ice extent and thickness (e.g., Park et al. 2015a, b; Woods and Caballero 2016; Mortin et al. 2016; Burt et al. 2016); an earlier melt onset for sea

✉ Marie C. McGraw
   mcmcgraw@uw.edu

[1] Department of Atmospheric Science, Colorado State University, Fort Collins, CO, USA

[2] Present Address: Department of Atmospheric Science, University of Washington, Seattle, WA, USA

[3] Present Address: Climate Prediction Center/NCEP/NWS/Innovim, LLC, College Park, MD, USA

[4] 14th Weather Squadron, United States Air Force, Asheville, NC, USA

ice (e.g., Park et al. 2015b; Mortin et al. 2016); changes in Arctic surface temperature variability (e.g., Woods et al. 2013; Messori et al. 2018); and an increase in upper ocean heat content (e.g., Park et al. 2015a). Moist intrusions into the Arctic are closely related to the midlatitude and tropical circulations through Rossby wave breaking and atmospheric blocking (e.g., Woods et al. 2013; Liu and Barnes 2015); transport by extratropical cyclones, especially in the North Atlantic region (e.g., Sorteberg and Walsh 2008; Dufour et al. 2016); atmospheric rivers (e.g., Newman et al. 2012; Baggett et al. 2016); planetary wave activity (e.g., Goss et al. 2016; Graversen and Burtu 2016; Franzke et al. 2016); and tropical convection (e.g., Lee 2014; Baggett and Lee 2017). Changes in moisture transport into the Arctic also have strong implications for the Arctic's future climate, as moisture transport into the Arctic is expected to increase in a warmer climate (e.g., Serreze and Barry 2005; Graversen 2006; Langen and Alexeev 2007). Thus, changes in circulation that affect Arctic moisture transport could directly impact future Arctic warming.

While the midlatitude circulation can substantially impact moisture transport into the Arctic, a warmer Arctic can alter the midlatitude circulation itself. In prior work, a warmer Arctic has been linked to changes in extreme temperature events (e.g., Screen et al. 2015; Ayarzagüena and Screen 2016), reductions in overall temperature variability (e.g., Screen 2014; Blackport and Kushner 2017), and an equatorward shift and weakening of the midlatitude jet streams (e.g., Deser et al. 2010; Butler et al. 2010; Screen et al. 2018), although the subtleties of these responses have been refined more recently (e.g. Peings et al. 2017; Ronalds et al. 2018; Zappa et al. 2018). Arctic warming has also been connected to changes in midlatitude sea level pressure and 500 hPa geopotential heights (e.g., Overland et al. 2015; Blackport and Kushner 2017; Screen et al. 2018; Zappa et al. 2018), planetary wave patterns (e.g., Francis and Vavrus 2015), and the warm Arctic-cold continents pattern (e.g., Kug et al. 2017), although some of these connections, particularly their discernability from internal variability, have been debated (e.g. Barnes 2013; Barnes and Screen 2015; McCusker et al. 2016; Sun et al. 2016; Cattiaux et al. 2016). Recent work has also suggested that the Arctic is capable of influencing the midlatitudes indirectly via changes in the stratospheric polar vortex (e.g., Sun et al. 2015; Wu and Smith 2016; Kretschmer et al. 2016). The Arctic's ability to influence the midlatitudes can be modulated by changes in the background state of the ocean (e.g., Deser et al. 2016; Screen and Francis 2016; Sung et al. 2016; Smith et al. 2017) and sea ice (e.g., Screen 2017; Screen et al. 2018). Ultimately, these changes in the midlatitude circulation can feed back upon the Arctic, further modifying Arctic weather and climate.

The midlatitude circulation can warm the Arctic via moisture intrusions, and changes in Arctic climate can modify the midlatitude circulation. Thus, if the Arctic can drive changes in the midlatitude circulation, do these changes in the midlatitude circulation further modify moisture transport into the Arctic? We explore this question using a set of atmosphere-only general circulation model simulations from Sun et al. (2015), described in more detail in Sect. 2. These experiments simulate the atmospheric response to changes in sea ice extent; thus, we focus on the role of sea ice extent in driving an atmospheric response that further modifies Arctic moisture fluxes. In Sect. 2, we define moisture transport into and out of the Arctic and briefly explain our Rossby wave breaking detection algorithm. In Sect. 3, we discuss our key results linking the response of the large-scale, midlatitude circulation to changes in Arctic moisture fluxes, including changes in the behavior of the eddy-driven jet and Rossby wave breaking. We summarize our results and conclude in Sect. 4.

2 Methods

2.1 Climate model experiments

Our analysis is conducted on the output of a pair of atmospheric general circulation model experiments performed by Sun et al. (2015). Both experiments use the Community Atmospheric Model, version 4 (CAM4), with a horizontal resolution of 1.9° latitude by 2.5° longitude, 26 vertical levels from the surface to 3.5 hPa, and prescribed stratospheric ozone. The first experiment, which we denote as CTRL (CONTROL in Sun et al. 2015), is forced with a prescribed sea ice concentration (SIC) and sea surface temperature (SST) that have been derived from the average over the years 1980–1999. The SIC and SST seasonal cycles are obtained from the average of a three-member ensemble of twentieth-century simulations of the fully coupled version of the Whole Atmosphere Chemistry-Climate Model (WACCM). The second experiment, which we denote as PERT (TOTAL in Sun et al. 2015), is forced with SIC derived from the years 2080–2099. The 2080–2099 SIC is calculated from a one-member fully coupled 21st century WACCM experiment under Representative Concentration Pathway 8.5 (RCP8.5) conditions, the scenario with highest warming carried out in the Climate Model Intercomparison Project, Version 5 (CMIP5) studies. The SSTs in PERT are identical to those in CTRL, except at gridpoints where the fractional sea ice cover in PERT is less than that of CTRL. In this case, SSTs are prescribed from an average of the 2080–2099 SSTs at that gridpoint from the WACCM RCP8.5 simulation. In both scenarios, sea ice has a prescribed thickness of 2 m, and there are no changes in Antarctic sea ice. We note that although sea ice thickness

is prescribed in these simulations, sea ice thinning may also have a substantial impact on the circulation, particularly in the winter months, due to a reduction in the sea ice's ability to insulate the atmosphere from the stronger and consequent increases in atmospheric temperature and water vapor (e.g., Burt et al. 2016; Lang et al. 2017; Labe et al. 2018; Blackport and Screen 2019); although recent work suggests that overall the circulation response is more sensitive to changes in sea ice concentration than it is to changes in sea ice thickness (e.g., Labe et al. 2018; Blackport and Screen 2019). In these simulations, we focus on the role of sea ice extent in driving changes in the midlatitude circulation that act to modify Arctic moisture transport; the sensitivity of this response to sea ice thickness is left to future work. We use 40 years of daily mean model output to explore the subseasonal circulation changes associated with sea ice loss. When we investigated the changes in the circulation with 60 years of daily mean model output, we drew similar conclusions. The difference in SIC (Fig. 1a) and 1000 hPa temperature (Fig. 1b) in the boreal cold season (September–February, hereafter SONDJF) between PERT and CTRL can be seen in Fig. 1. In Fig. 1 and subsequent figures, significant changes between PERT and CTRL are assessed at 95% confidence using a two-sided student's t test. In these figures, only gridpoints with significant changes are plotted. We note that when we assess significance with the nonparametric Wilcoxon signed-rank test, our results are very similar; for simplicity, we show only the results assessed with the student's t test.

The CAM4 simulations analyzed here are low-top simulations—that is, their highest pressure level is only at 3.5 hPa. Moreover, their vertical resolution is relatively coarse, meaning that CAM4's stratospheric dynamics are not as well-resolved as those in a high-top model like WACCM. These features are noteworthy, as prior studies have found that the stratospheric polar vortex can influence the tropospheric response to sea ice loss and Arctic warming (e.g., Peings and Magnusdottir 2014; Kim et al. 2014; Feldstein and Lee 2014; Wu and Smith 2016). However, a comparison between the low-top CAM4 and the high-top WACCM indicates that, while the magnitude of the tropospheric response to sea ice loss is weaker in CAM4 as compared to WACCM, the overall pattern of the response is similar in both models (Sun et al. 2015). In addition, previous work has highlighted the importance of planetary-scale wave activity, as well as primarily tropospheric phenomena in understanding the atmospheric circulation response to sea ice loss (e.g., McKenna et al. 2018). Therefore, our analysis is conducted under the assumption that the overall structure of the circulation and moisture flux responses to sea ice loss are largely robust to using the low-top model versus the high-top model.

2.2 Defining IVT

In this work, moisture transport is measured using vertically integrated water vapor transport (IVT). IVT is calculated according to Mundhenk et al. (2016),

$$IVT = \left(\frac{1}{g} \int_{1000}^{300} uq\,dp\right)\hat{i} + \left(\frac{1}{g} \int_{1000}^{300} vq\,dp\right)\hat{j}, \tag{1}$$

where g is the gravitational acceleration, u is zonal wind, v is meridional wind, q is specific humidity, and dp is the pressure difference between adjoining pressure levels. Here, we integrate from 1000 to 300 hPa, but IVT is not highly sensitive to the upper or lower boundaries of the integral, as the largest values of water vapor are primarily confined to the lowest levels of the atmosphere, and the largest contributions to IVT derive from the ocean basins. In Fig. 2, we diagnose the change in total moisture transport into and out of the Arctic by focusing only on the meridional ($\hat{j}$) component of IVT averaged along 70° N, which we will simply refer to as meridional IVT. We will also decompose meridional IVT into poleward and equatorward components. In this decomposition, poleward IVT refers to the daily average of vq across all grid points along 70° N such that we set $vq = vq$ at grid points where $v > 0$ and $vq = 0$ at grid points where $v \leq 0$. Conversely, we define equatorward IVT as the daily average of vq across all points along 70° N such that $vq = vq$ at grid points where $v \leq 0$ and $vq = 0$ at grid points where $v > 0$.

2.3 Rossby wave breaking algorithm

Rossby wave breaking events are identified with the algorithm of Liu et al. (2014), which is based on that of Strong and Magnusdottir (2008). Briefly, potential temperature is interpolated to the 2-potential vorticity unit (PVU, 1 PVU = 10^{-6} K kg^{-1} m^{-2} s^{-1}) surface. The 2-PVU surface serves as an approximation for the tropopause in the extratropics and is useful for diagnosing Rossby wave breaking events (e.g. Franzke et al. 2011; Liu and Barnes 2015). The algorithm diagnoses Rossby wave breaking events by identifying regions of overturning potential temperature contours on the 2-PVU surface whose enclosed areas exceed a certain threshold (i.e., greater than 25° in an equirectangular projection). The Rossby wave breaking events are calculated based only on the surface area of the overturning potential temperature contours—there is no measure of the strength of the overturning. The Rossby wave breaking events are classified as anticyclonic or cyclonic wave breaking events based on their direction of overturning. In the Northern Hemisphere, anticyclonic Rossby wave breaking events occur when cresting waves are tilted in a southwest to

Fig. 1 a Change (PERT-CTRL) in percent of grid box covered by sea ice for associated with sea ice loss in SONDJF. **b** Change (PERT-CTRL) in 1000 hPa temperature. Only gridpoints where the changes in temperature are significant at 95% confidence are shaded. Black contours show the 1000 hPa temperature in CTRL, contoured every 20 K from 260 to 300 K

(a) Change in Ice Coverage (SONDJF)

(b) Change in 1000 hPa Temperature (SONDJF)
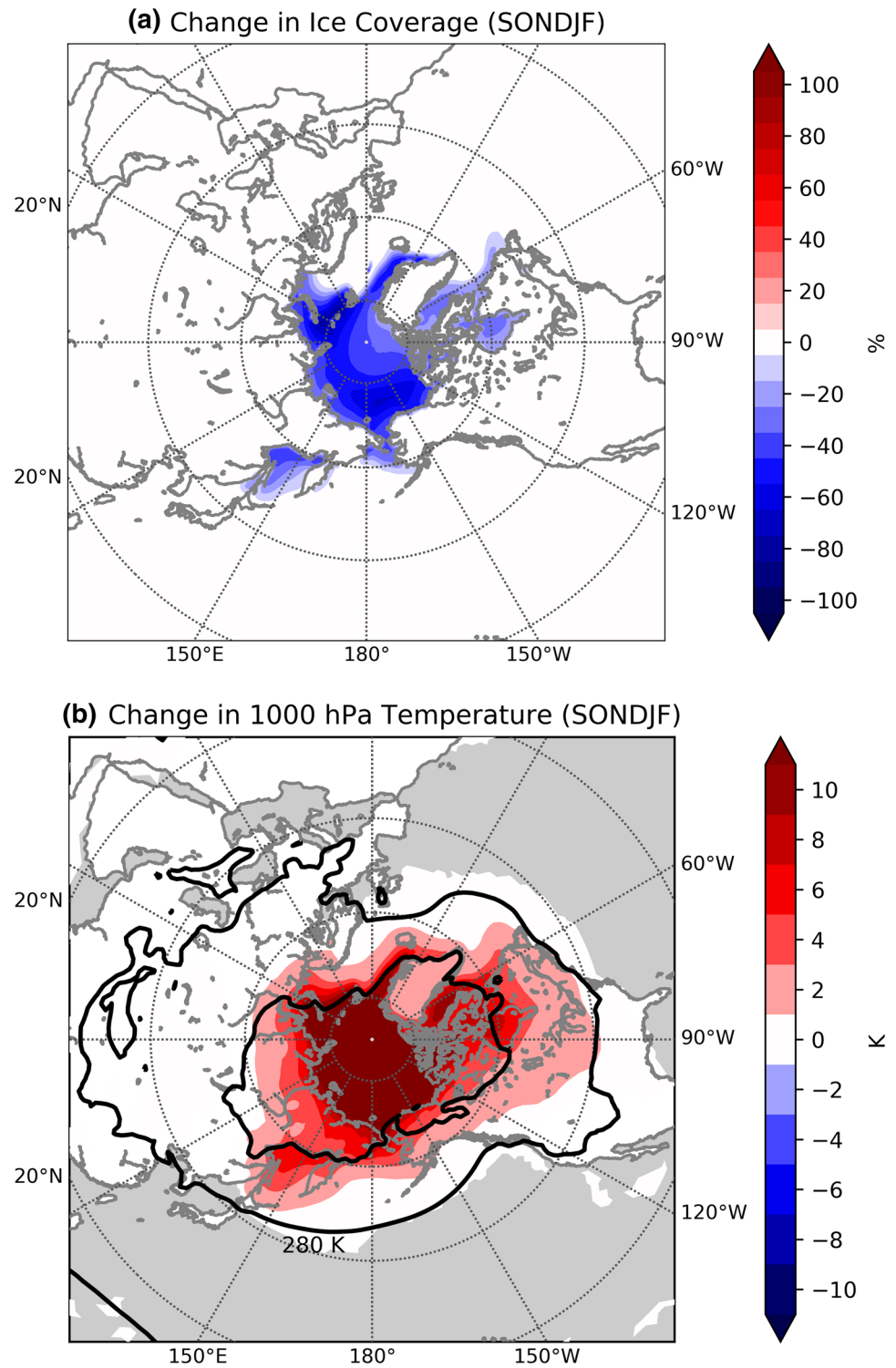
northeast orientation and overturn in a clockwise direction. Cyclonic Rossby wave breaking events occur when cresting waves are tilted in a southeast to northwest orientation and overturn in a counterclockwise direction (see Figure 5 in Liu and Barnes (2015) for an example of each).
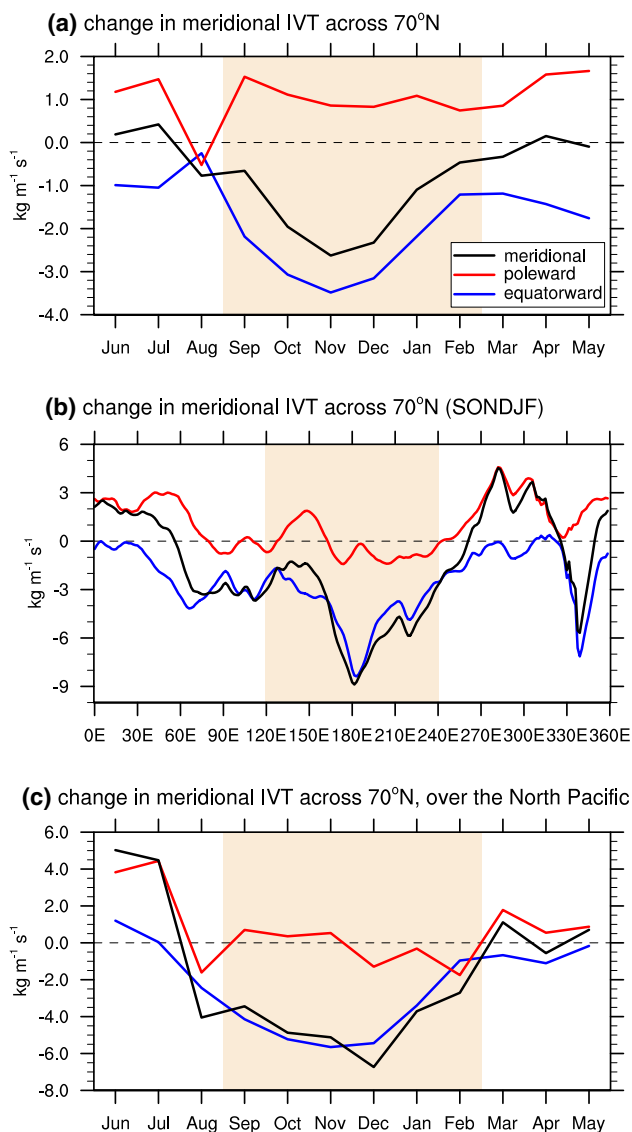
(a) change in meridional IVT across 70°N

(b) change in meridional IVT across 70°N (SONDJF)

(c) change in meridional IVT across 70°N, over the North Pacific

Fig. 2 Change (PERT-CTRL) in meridional IVT associated with sea ice loss as a function of **a** month, **b** longitude during SONDJF (highlighted in **a**), and **c** month over the North Pacific region (120°–240°E, highlighted in **b**). Red lines indicate poleward (northward) IVT, blue lines indicate equatorward (southward) IVT, and black lines are the meridional IVT (poleward IVT + equatorward IVT)

3 Results

3.1 Changes in meridional IVT

The seasonal and longitudinal variability of meridional IVT across 70° N is explored in Fig. 2. Figure 2 shows the changes in total meridional (black lines), poleward (red lines), and equatorward (blue lines) IVT across 70° N associated with sea ice loss (that is, PERT-CTRL). The results of Fig. 2 are not highly sensitive to the 70° N boundary and are broadly similar for 65° N and 60° N (not shown). Poleward

IVT increases in PERT as compared to CTRL (red line in Fig. 2a), particularly in September–February (SONDJF). This increase in poleward IVT into the Arctic suggests a positive relationship between sea ice loss and moisture fluxes, in which sea ice loss (Fig. 1a) is associated with an increase in moisture transport into the Arctic, which could lead to an increase in downwelling longwave radiation and warmer Arctic temperatures. However, PERT also shows an increase in equatorward IVT across 70° N—that is, moisture flux *out* of the Arctic (blue line in Fig. 2a). The equatorward IVT actually increases *more* than the poleward IVT.

When meridional IVT across 70° N is broken down by longitude (Fig. 2b) during SONDJF, it is clear that much of the increase in equatorward IVT (blue line in Fig. 2b) occurs in the North Pacific region (120° E–240° E, indicated by the orange shading in Fig. 2b), with about 54% of the total equatorward IVT in SONDJF occurring between 120° and 240° E. As with the Northern Hemisphere mean, this change in equatorward moisture flux in the North Pacific is greatest in SONDJF (blue line in Fig. 2c). These changes in meridional IVT (vq) can be further understood by breaking down vq into time and zonal means, and their respective anomalies. The time-mean meridional vapor transport, $\overline{vq}$, is decomposed following equation 4.9 of Peixóto and Oort (1992),

$$\overline{vq} = \overline{v} \cdot \overline{q} + \overline{v'q'} = [\overline{v}] \cdot [\overline{q}] + [\overline{v}] \cdot \overline{q}^* + \overline{v}^* \cdot [\overline{q}] + \overline{v}^* \cdot \overline{q}^* + \overline{v'q'},$$
(2)

where $\cdot$ is the time-mean (defined using calendar-month means), [ ] represents the zonal-mean, ' represents the deviations from the time-mean, and * indicates deviations from the zonal-mean. Taking the zonal-mean of Eq. 2 yields,

$$[\overline{vq}] = [\overline{v}] \cdot [\overline{q}] + [\overline{v}^* \cdot \overline{q}^*] + [\overline{v'q'}],$$
(3)

Equation 3 breaks the time-mean, zonal-mean meridional vapor transport into three terms: a component associated with the mean meridional circulation (MMC, $[\overline{v}] \cdot [\overline{q}]$), a component associated with the stationary eddies ($[\overline{v}^* \cdot \overline{q}^*]$), and a component associated with transient eddies ($[\overline{v'q'}]$). Figure 3 shows each of these three components—mean meridional, stationary, and transient—separately (yellow, blue, and red lines in Fig. 3a, respectively). Figure 3a demonstrates that the change in $[\overline{vq}]$ associated with sea ice loss (black line) is largely dominated by the changes in the transient vapor transport $[\overline{v'q'}]$. We will return to the significance of the transient vapor transport in the discussion of Rossby wave breaking events in Sect. 3.3

In Fig. 3b, we examine $\overline{vq}$ as a function of longitude (Eq. 2) during SONDJF. Equation 2 indicates that the moisture transport can be divided into a term that describes the advection of the background moisture by the stationary winds ($\overline{v}^* \cdot [\overline{q}]$; dashed blue line in Fig. 3b), and a term that
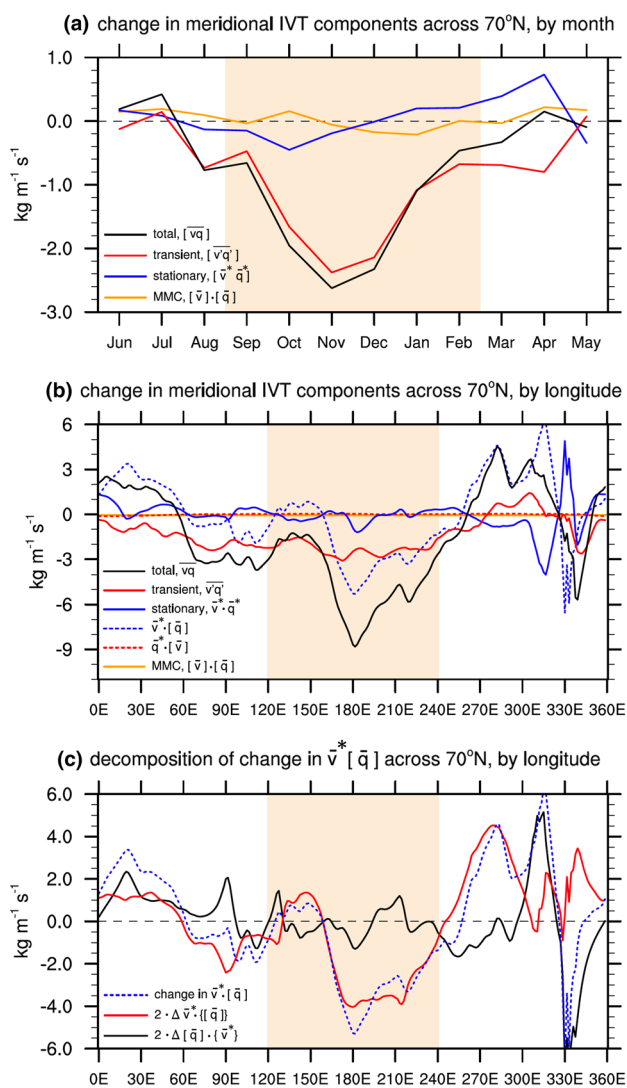
(a) change in meridional IVT components across 70°N, by month

(b) change in meridional IVT components across 70°N, by longitude

(c) decomposition of change in $\overline{v}^*\,[\overline{q}]$ across 70°N, by longitude

Fig. 3 Change (PERT-CTRL) in the components of meridional IVT during SONDJF associated with sea ice loss as a function of **a** month (SONDJF is highlighted in orange), and **b** longitude (the North Pacific is highlighted in orange). In **a**, black lines indicate the change in meridional IVT, yellow lines indicate the change in meridional IVT associated with the mean meridional circulation (MMC), red lines indicate the change in meridional IVT associated with the transient waves, and blue lines indicate the change in meridional IVT associated with the stationary waves. In **b**, the circulation is broken down further into $\overline{v}^* \cdot [\overline{q}]$ (the advection of background moisture by the stationary meridional winds; dotted blue line) and $\overline{q}^* \cdot [\overline{v}]$ (the advection of the stationary moisture field by the background wind; dotted red line). **c** The decomposition of $\overline{v}^* \cdot [\overline{q}]$ into a component associated with the change in meridional winds ($\Delta\overline{v}^* \cdot \{[\overline{q}]\}$, red line) and a component associated with the change in atmospheric water vapor ($\Delta[\overline{q}] \cdot \{\overline{v}^*\}$, black line); orange highlighting indicates the North Pacific

describes the advection of the stationary moisture field by the background meridional winds ($\overline{q}^* \cdot [\overline{v}]$; dashed red line in Fig. 3b). Figure 3b clearly suggests that the advection of the background moisture by the stationary winds ($\overline{v}^* \cdot [\overline{q}]$;

dashed blue line) is a much greater contributor to the total change in meridional IVT (black line) than the advection of the stationary moisture field by the background wind ($\overline{q}^* \cdot [\overline{v}]$).

Figure 3b emphasizes the importance of $\overline{v}^* \cdot [\overline{q}]$ (the advection of the background moisture by the stationary winds). However, this term could be dominated by either the changes in the background moisture ($[\overline{q}]$) or changes in the stationary meridional winds ($\overline{v}^*$). Thus, we further break down the change in $\overline{v}^* \cdot [\overline{q}]$,

$$\overline{v}^* \cdot [\overline{q}]|_{PERT} - \overline{v}^* \cdot [\overline{q}]|_{CTRL} = 2\Delta\overline{v}^* \cdot \{[\overline{q}]\} + 2\{\overline{v}^*\} \cdot \Delta[\overline{q}],$$
(4)

where the { } indicates the average of both CTRL and PERT (that is, $\{A\} = \frac{A_{PERT} + A_{CTRL}}{2}$), and the Δ indicates half of the difference between PERT and CTRL (that is, $\Delta A = \frac{A_{PERT} - A_{CTRL}}{2}$). Thus, the change in $\overline{v}^* \cdot [\overline{q}]$ (Eq. 4) can be expressed as the sum of two terms, where the first term represents the change in moisture advection due to the change in stationary winds ($\Delta\overline{v}^* \cdot \{[\overline{q}]\}$; red line in Fig. 3c), and the second term represents the change in moisture advection due to the change in background moisture ($\{\overline{v}^*\} \cdot \Delta[\overline{q}]$; black line in Fig. 3c). Figure 3c demonstrates that first term dominates, particularly over the North Pacific (highlighted by the orange box in Fig. 3c), emphasizing the importance of the changes in the meridional winds. That is, the change in meridional IVT derives principally from a change in the circulation rather than background moisture increases associated with sea ice loss.

Figures 2 and 3 explore the seasonal and geographic variability of meridional IVT across 70° N, and break meridional IVT down across temporal and spatial scales. We see that the largest changes in meridional IVT across 70° N occur in the boreal cold season (SONDJF, Fig. 2a), and over the North Pacific (120°–240° E, Fig. 2b). A decomposition of meridional moisture transport (Eqs. 2–3) highlights the role of the transient eddies, and the stationary meridional winds as important components of the overall change in meridional IVT (Fig. 3b, c). Thus, changes in the circulation associated with sea ice loss are responsible for at least part of the increase in equatorward moisture transport through 70° N. With this in mind, we explore changes in the circulation that could explain Figs. 2, 3 and 4.

3.2 Changes in large-scale circulation

In Figs. 4, 5 and 6, we examine changes in the circulation associated with sea ice loss (PERT-CTRL) during SONDJF by focusing on 850 and 300 hPa zonal winds and 500 hPa geopotential heights (Z500).

The change in zonal winds at lower (850 hPa, Fig. 4a) and upper (300 hPa, Fig. 4b) levels associated with sea ice loss is seen in Fig. 4. At both 850 and 300 hPa, the largest

Fig. 4 Change (PERT-CTRL) in zonal winds in SONDJF for **a** 850 hPa and **b** 300 hPa. Only gridpoints where the changes in zonal winds are significant at 95% confidence are shaded. Black contours show the zonal winds in CTRL, contoured every 5 m s^{-1} from − 10 to + 10 m s^{-1} in **a**, and every 10 m s^{-1} from 10 to 40 m s^{-1} in **b**

(a) Change in 850 hPa Zonal Winds (SONDJF)

(b) Change in 300 hPa Zonal Winds (SONDJF)
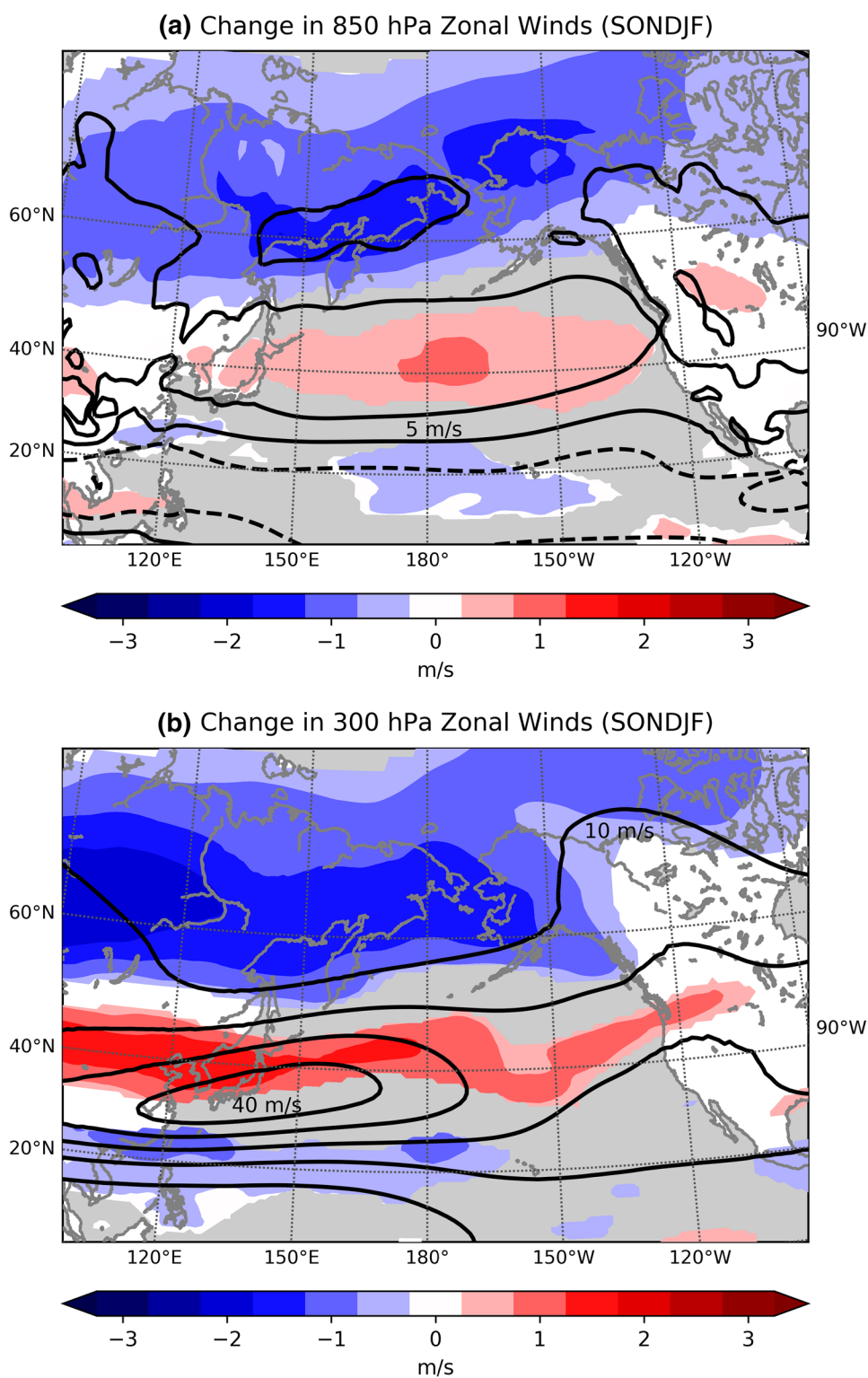
changes in zonal winds occur poleward of the jet, with a substantial weakening of the winds poleward of about 55° N, and a narrowing and small equatorward shift of the jet (as defined by Woollings et al. 2010). This weakening of the winds on the poleward flank and small equatorward shift of the jet is consistent with recent work associating sea ice loss and Arctic warming with a narrowing of the eddy-driven jet, rather than a pure shift, and a reduction in winds poleward of the jet (e.g., Peings et al. 2017; Ronalds et al. 2018; Zappa et al. 2018). This broad weakening of

Fig. 5 Change (PERT-CTRL) in cyclonic wind shear $\left(-\frac{\partial u}{\partial y}\right)$ at **a** 850 hPa and **b** 300 hPa. Only gridpoints where the changes in wind shear are signifiant at 95% confidence are shaded

(a) Change in 850 hPa Cyclonic Wind Shear (SONDJF)

(b) Change in 300 hPa Cyclonic Wind Shear (SONDJF)
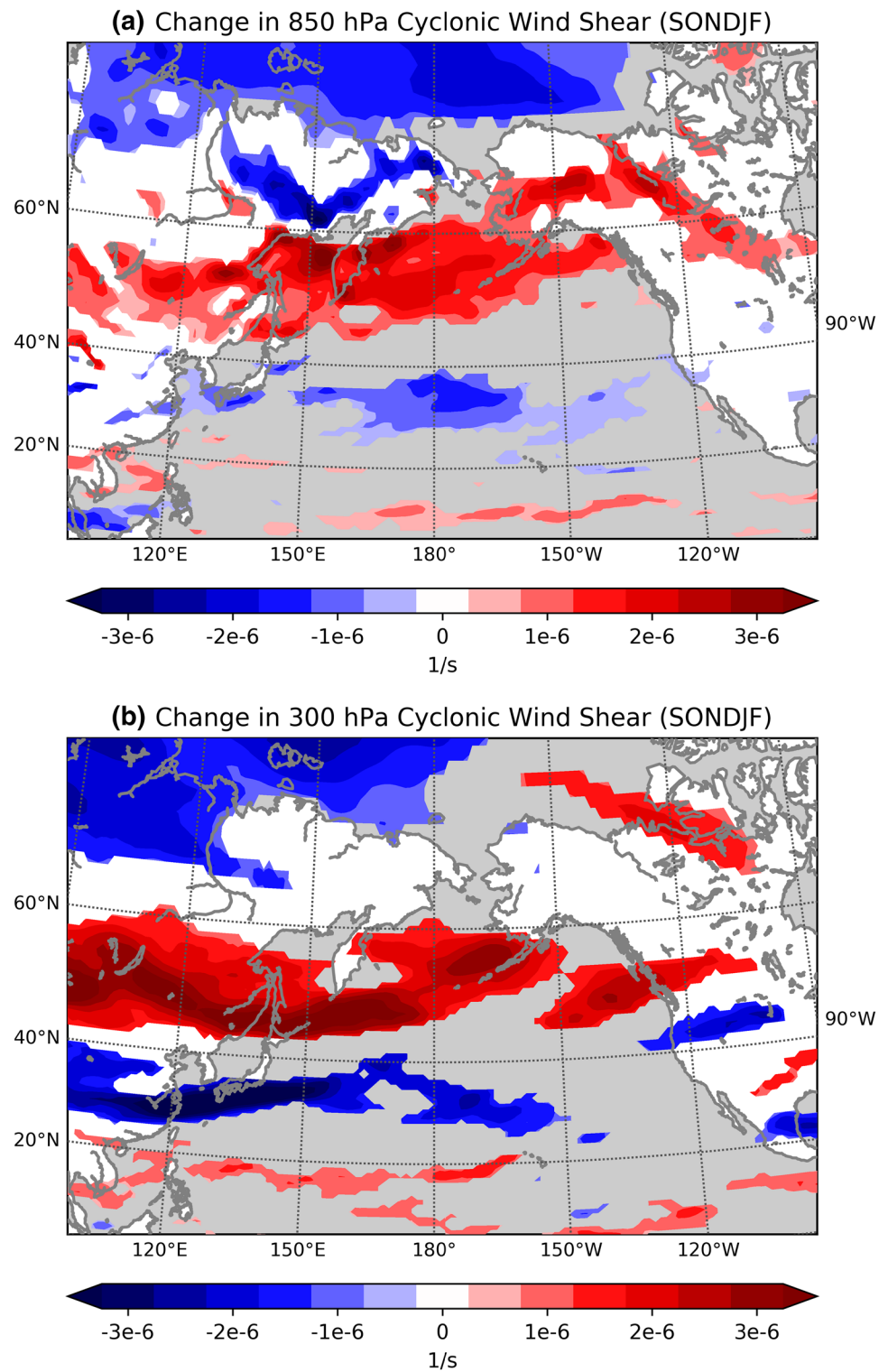
the zonal winds on the poleward flank of the jet has implications for the wind shear $\left(-\frac{\partial u}{\partial y}\right)$. As expected from Fig. 4, the cyclonic wind shear increases between about 40°–60° N at both 850 hPa (Fig. 5a) and 300 hPa (Fig. 5b). These increases are especially pronounced in the center and western portions of the Pacific, particularly at 300 hPa. This increase in cyclonic wind shear will be linked to changes in Rossby wave breaking in the next section.

Fig. 6 **a** Change (PERT-CTRL) in 500 hPa geopotential height in SONDJF. **b** as in **a**, but with the zonal mean removed. Only gridpoints where the changes in 500 hPa geopotential height are signifiant at 95% confidence are shaded. Black contours in **a** show the geopotential heights in CTRL (contoured every 100 m from 5200 to 5800 m); and in **b**, with their zonal means removed (contoured every 50 m from −150 to +100 m)

(a) Change in 500 hPa Geopotential Height (SONDJF)

(b) Change in Zonal Anomalies of 500 hPa Geopotential Height (SONDJF)
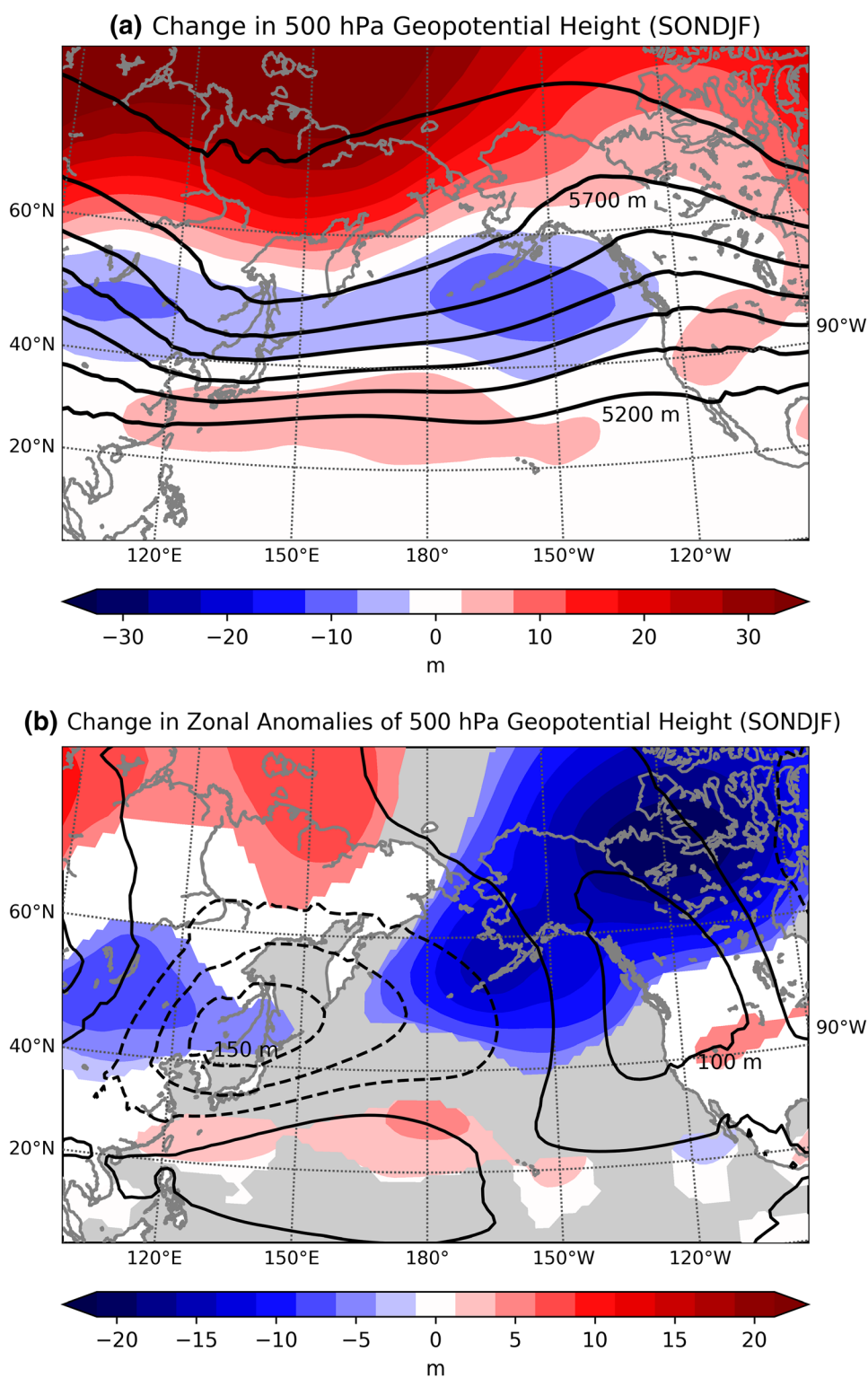
As moisture fluxes are largely driven by the mid-level steering pattern, we now turn our attention to the changes in 500-hPa geopotential height ($Z500$) associated with sea ice loss (colored shading in Fig. 6). As expected, the geopotential height changes over the Arctic are positive, corresponding to the temperature increases there (Fig. 1b). In contrast, Z500 decreases over interior east Asia, and the eastern half of the North Pacific. Removing the zonal mean component of $Z500$ further emphasizes the role of the zonally asymmetric circulation (Fig. 6b), whose importance is

Fig. 7 Change (PERT-CTRL) in SONDJF Rossby wave breaking frequency for **a** cyclonic wave breaking and **b** anticyclonic wave breaking events. Only gridpoints where the changes in wave breaking frequency are significant at 95% confidence are shaded. Black contours show the **a** cyclonic and **b** anticyclonic Rossby wave breaking frequency in CTRL, contoured every 5% from 5 to 30%. The blue box in **a** indicates the area encompassing 40°–70° N, 150°–200° E

(a) Change in Cyclonic Rossby Wave Breaking Frequency (SONDJF)

(b) Change in Anticyclonic Rossby Wave Breaking Frequency (SONDJF)
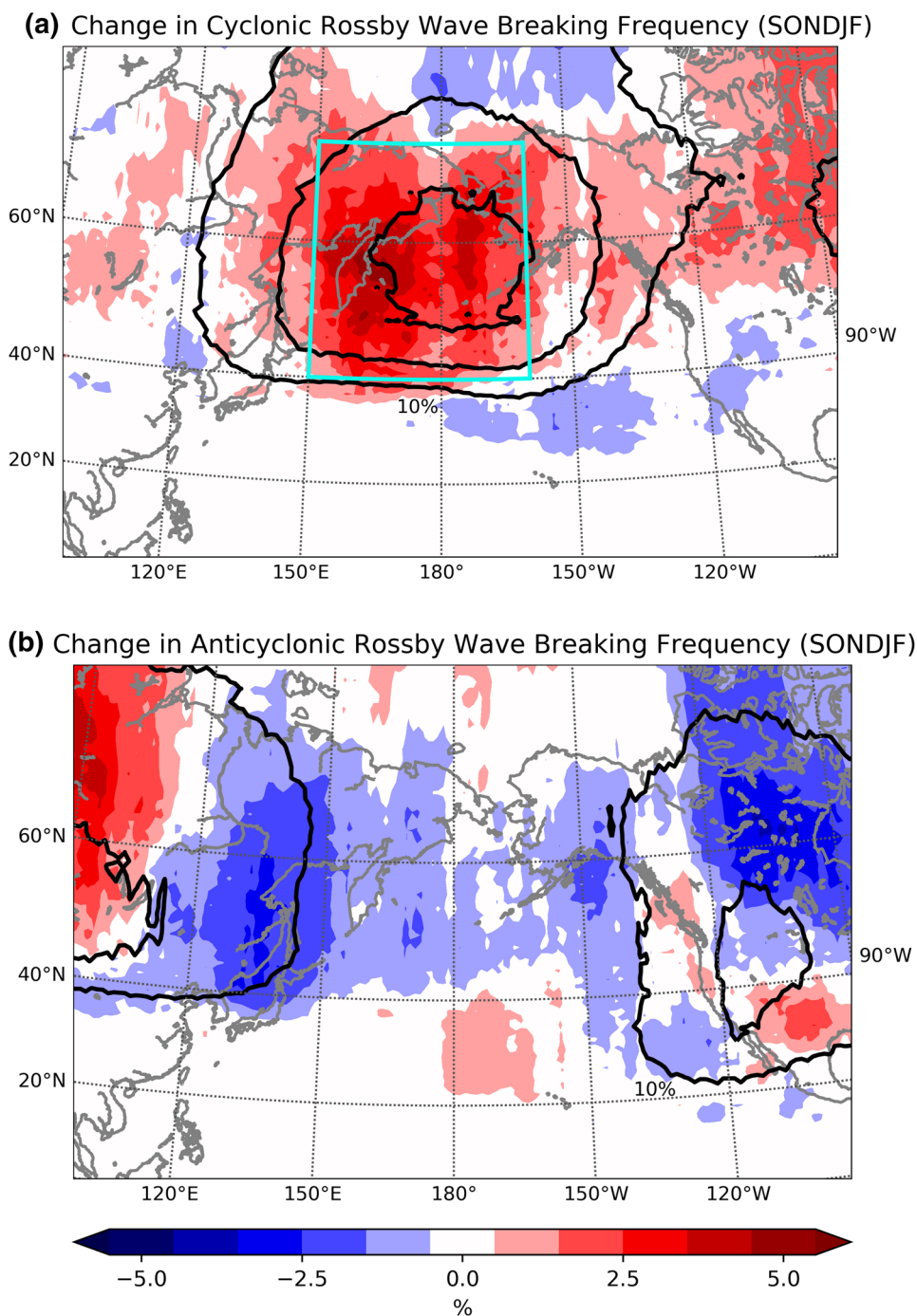
highlighted in Fig. 3, where it was shown that changes in $\overline{v}^* \cdot [\overline{q}]$ dominate in the North Pacific. Figure 6b highlights a weakening of the west–east gradient in the zonally asymmetric component of Z500 over the North Pacific. In PERT, compared to CTRL, the heights rise to the west of the dateline and fall to the east of the dateline. These height changes result in a weakened west–east gradient that is consistent with less meridional transport into the Arctic over the North Pacific as seen in Fig. 2b.

3.3 Changes in Rossby wave breaking

Thus far, we have observed that there is an increase in equatorward moisture flux (out of the Arctic) associated with sea ice loss over the North Pacific during SONDJF (Fig. 2). A decomposition of meridional IVT reveals that processes that occur on transient timescales describe most of this increase in equatorward moisture transport (Fig. 3a) and that changes in the circulation have a substantial impact on the total moisture transport (Fig. 3b, c). An analysis of changes in the

large-scale circulation associated with sea ice loss reveals the following:

- a substantial weakening of the zonal winds poleward of the jet at both lower and upper levels (Fig. 4);
- an increase in cyclonic wind shear at lower and upper levels, as expected from the weakening of the zonal winds poleward of the jet (Fig. 5);
- an increase in $Z500$ over the polar cap and a decrease in $Z500$ over Alaska (Fig. 6); and,
- a weakened west–east gradient in $Z500$ between far-eastern Russia and the Bering Strait that is particularly apparent in the zonally asymmetric component of $Z500$ (Fig. 6).

These changes in the circulation suggest that Rossby wave breaking could be driving the changes in the meridional moisture transport. Specifically, the increase in cyclonic wind shear on the poleward flank of the jet (Fig. 5) suggests a corresponding increase in cyclonic Rossby wave breaking in this region (e.g., Thorncroft et al. 1993; Tyrlis and Hoskins 2008), as increases in cyclonic Rossby wave breaking have also been associated with equatorward shifts of the jet (e.g., Riviére 2011; Barnes and Hartmann 2012; Liu and Barnes 2015). Additionally, Rossby wave breaking events occur on the transient timescales emphasized in Fig. 3, further highlighting the possibility of changes in Rossby wave breaking being associated with the increase in equatorward IVT in PERT.

When we calculate the changes in Rossby wave breaking frequency associated with sea ice loss (Fig. 7), it is clear that there is an increase in cyclonic Rossby wave breaking frequency in the North Pacific (Fig. 7a) and a corresponding decrease in anticyclonic Rossby wave breaking in the same region (Fig. 7b). Furthermore, the largest increase in cyclonic Rossby wave breaking occurs on the eastern edge of the Bering Sea, near Kamchatka—corresponding to large increases in cyclonic wind shear (Fig. 5) and the strongest climatological gradient in $Z500$, particularly in the zonally asymmetric component of $Z500$ (Fig. 6). Thus, the increase in cyclonic Rossby wave breaking, and a slight westward shift of wave breaking activity compared with CTRL, corresponds with increases in cyclonic wind shear, a narrower and equatorward-shifted jet, and the location of the maximum climatological gradient in $Z500$.

While Figs. 4, 5, 6 and 7 seemingly present a cohesive picture of changes to the large-scale circulation, it must be asked: are the wave breaking events actually driving the moisture fluxes observed in Figs. 2 and 3, or are they simply coincident with the change in meridional IVT? We address this question by creating lagged composites of moisture transport during cyclonic Rossby wave breaking events. Cyclonic Rossby wave breaking events are classified first
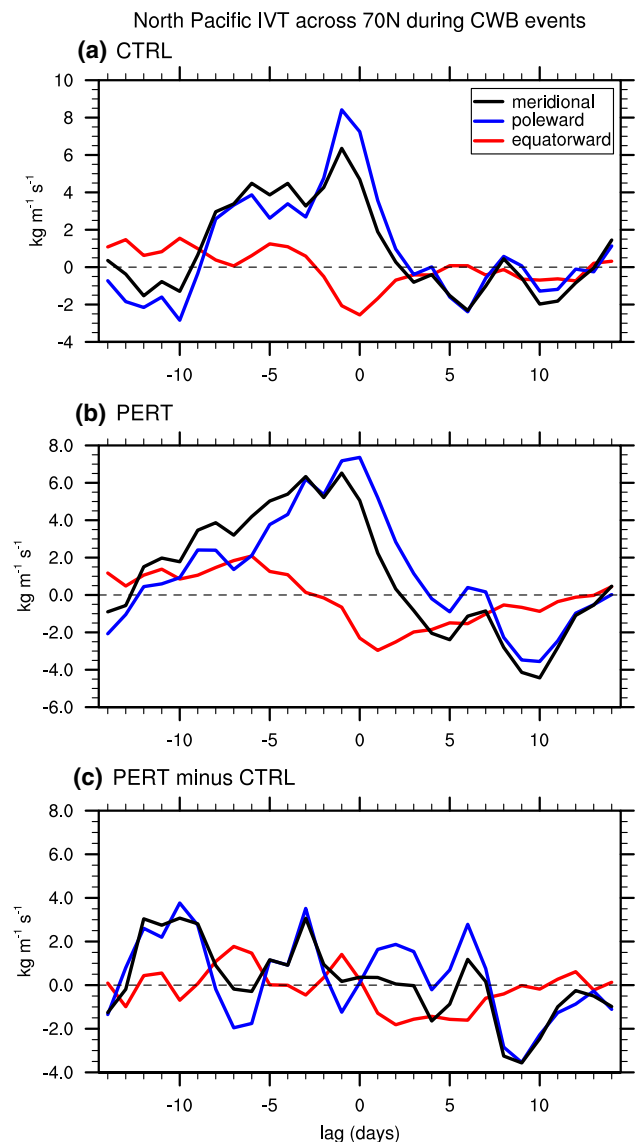

Fig. 8 Lagged composites of anomalous moisture transport across 70° N over the North Pacific during cyclonic wave breaking (CWB) events for **a** CTRL, **b** PERT, and **c** PERT-CTRL. See Sect. 3.3 for a definition of events

by identifying days when cyclonic Rossby wave breaking anomalies exceed one standard deviation over the box 40° –70° N, 150°–200° E (indicated by the blue lines in Fig. 7a). Then, only days with the highest amplitude, separated by 28 days from each other, are retained and called cyclonic Rossby wave breaking events. Meridional IVT across 70° N, averaged between 120° and 240° E, is composited at lag days −14 to +14 against these events, and divided into poleward and equatorward IVT components. The results shown in Fig. 8 are not sensitive to the exact boundaries of the regions over which IVT and Rossby wave breaking are calculated. Figure 8 shows these anomaly composites for CTRL (Fig. 8a), PERT (Fig. 8b), and for their difference (Fig. 8c),

Z500 and **IVT** Composited on Cyclonic Rossby Wave Breaking Events
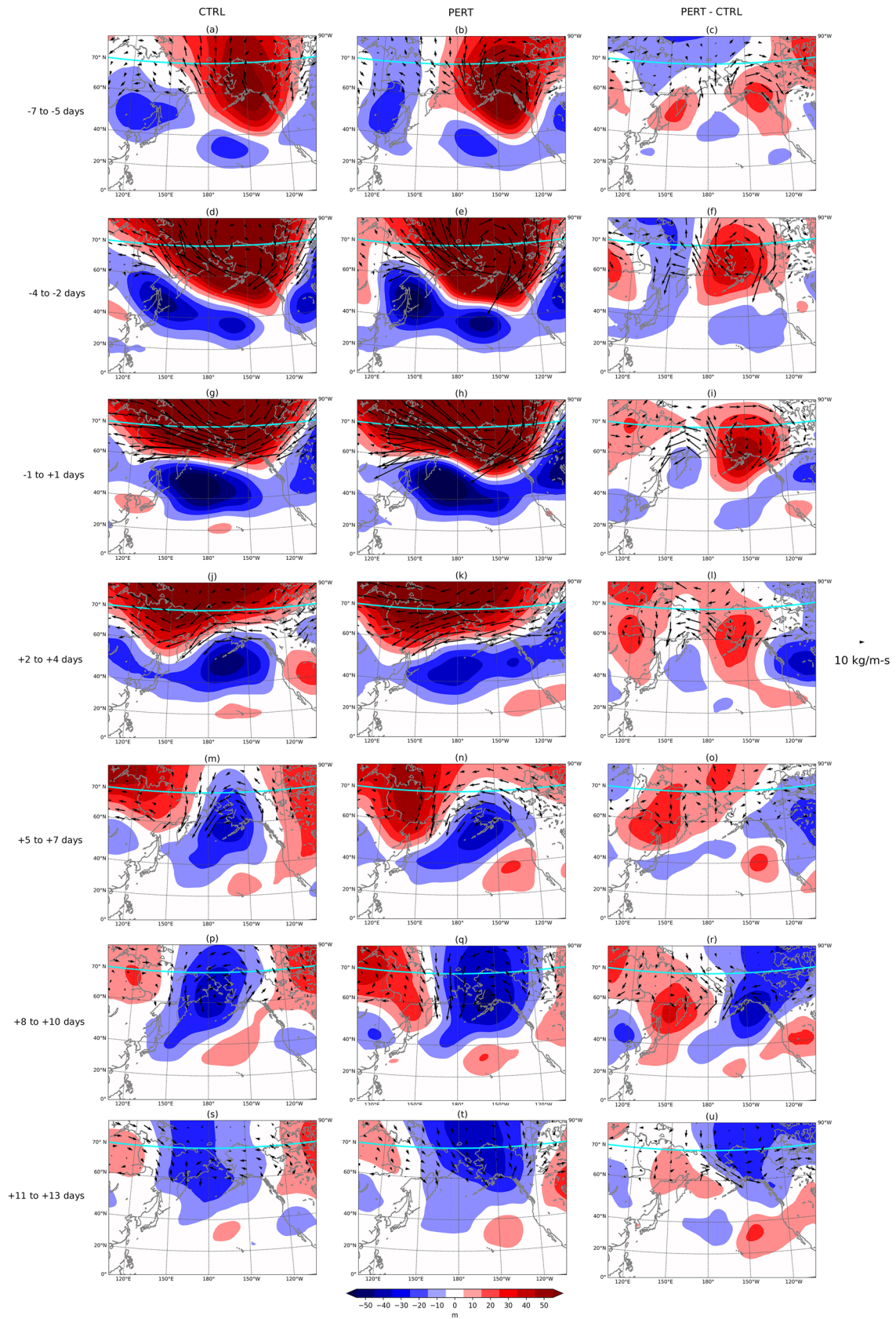
◀ **Fig. 9** Lagged composites of 500 hPa geopotential height (shading) and IVT (arrows; only plotted north of 60° N) anomalies during cyclonic Rossby wave breaking (CWB) events for (left) CTRL, (center) PERT, and (right) PERT-CTRL. Lag days are averaged in 3 day increments and begin at lag days − 7 to − 5 (before the event maximum, top row) and continue to lag days + 11 to + 13 (after the event maximum; bottom row). Only gridpoints with significant changes in 500 hPa geopotential height (IVT; only one component must be significant) are shaded (plotted). The solid cyan line indicates 70° N

as well as the variability of both poleward and equatorward moisture fluxes throughout the wave breaking lifecycle.

Previous work (e.g., Liu and Barnes 2015) has linked cyclonic Rossby wave breaking with more moisture transport into the Arctic. Thus, the results shown here may at first glance seem counterintuitive—linking cyclonic Rossby wave breaking with moisture transport *out* of the Arctic. However, Fig. 8 clearly indicates that cyclonic Rossby wave breaking events are associated with increases in poleward IVT (blue lines in Fig. 8a–c) shortly before and during the peak of the events, which is in concordance with the results of Liu and Barnes (2015). After the peak of the events, there is enhanced equatorward IVT (red lines in Fig. 8a–c; values of moisture transport that are less than zero indicate an *increase* in equatorward moisture transport), which is especially the case in PERT as compared to CTRL. The net meridional transport (black lines in Fig. 8a–c) follows the equatorward IVT (red lines)—the net IVT after the event peak (lag days 0 to + 14) is negative, indicating net equatorward transport. The net IVT becomes even more negative (more equatorward) in PERT as compared to CTRL, indicating that sea ice loss is associated with enhanced equatorward IVT following the peak of the Rossby wave breaking event cycle. We hypothesize that this enhanced equatorward moisture transport in PERT could be related to small but important changes in the circulation. Figure 7a shows that the maximum in cyclonic Rossby wave breaking activity shifts slightly westward in PERT relative to CTRL. The changes in cyclonic wind shear (Fig. 5) and Z500 (Fig. 6) also support a westward shift.

In order to investigate this hypothesis, we create lagged composites of Z500 and IVT anomalies over the North Pacific during the cyclonic Rossby wave breaking life cycle. Panels in Fig. 9 show 3-day running means of Z500 and IVT anomalies for cyclonic Rossby wave breaking events, ranging from lag days − 7 to + 13. In the days preceding cyclonic Rossby wave breaking events, PERT and CTRL show broadly similar patterns, with some small differences. Both CTRL and PERT show high Z500 anomalies over Alaska and the east Pacific and low Z500 anomalies over east Asia and the west Pacific (Fig. 9a, b), although these anomalies are slightly stronger in PERT. The overall changes (PERT-CTRL) in IVT around 70° N are relatively small up to 2 days before the cyclonic wavebreaking event (Fig. 9c,

f). By lag days − 4 to − 2, both CTRL and PERT show the development and strengthening of low height anomalies in the central subtropical Pacific, as well as over Japan and the Sea of Okhotsk (Fig. 9d, e), and a high Z500 anomaly over Alaska and the east Pacific.

By the event peak (lag days − 1 to + 1; Fig. 9g–i), the low height anomaly over the western Pacific has strengthened. The center of the low height anomaly is westward in PERT relative to CTRL (Fig. 9g, h), while the high height anomaly over Alaska is larger in PERT (Fig. 9i). As expected from Fig. 8, and from previous work (e.g. Liu and Barnes 2015), Fig. 9g, h show IVT directed poleward at the event peak in CTRL and in PERT, but it is weaker in PERT. In both cases, the strongest IVT is largely coincident with the strongest gradient in Z500.

The differences between CTRL and PERT become more pronounced after the peak of the cyclonic Rossby wave breaking event (lag days + 2 to + 13, Fig. 9j–u). At lag days + 2 to + 4 (Fig. 9j–l), both CTRL and PERT show a deepening of heights associated with the Aleutian low. The maximum Z500 anomaly is actually slightly stronger in CTRL than in PERT, and PERT shows stronger positive Z500 anomalies over Alaska as compared to CTRL (Fig. 9j–l). By lag days + 5 to + 7, these height anomalies have set up a west–east dipole in Z500, with anomalously high heights over eastern Russia and anomalously low heights over Alaska (Fig. 9m, n). This dipole is more pronounced in PERT than it is in CTRL, particularly the low height anomaly over Alaska (Fig. 9o). The west–east dipole in Z500 persists into lag days + 8 to + 10 (Fig. 9p, q), with stronger Z500 anomalies in PERT as compared to CTRL. These stronger Z500 anomalies in PERT create an anomalous west–east gradient in Z500 that maximizes over eastern Russia and Kamchatka, enhancing equatorward-directed IVT across 70° N in this region in PERT relative to CTRL (Fig. 9r). By lag days + 11 to + 13, a large low Z500 anomaly remains in PERT, while it is diminished in CTRL (Fig. 9s, t). Again, the larger, more persistent low Z500 anomaly in PERT is associated with anomalously large equatorward-directed IVT in the western Pacific, over eastern Russia and Kamchatka (Fig. 9u). Therefore, broadly speaking, after the peak of the cyclonic Rossby wave breaking life cycle, PERT shows stronger, more zonally extensive, and more persistent low Z500 anomalies over Alaska and the Bering Sea (similar to Fig. 6) when compared to CTRL (Fig. 9m–u). This stronger and more persistent low Z500 anomaly in PERT facilitates the development of a stronger west–east in Z500 that is associated with enhanced equatorward-directed IVT over the Bering Strait and eastern Siberia (Fig. 9m–u). Overall, a life cycle analysis of cyclonic Rossby wave breaking events reinforces the hypothesis that changes in the large-scale circulation associated with sea ice loss act to preferentially enhance equatorward moisture flux, particularly in the Bering Strait region.

4 Conclusions

We use the atmosphere-only general circulation model runs of Sun et al. (2015) to explore the changes in moisture flux across 70° N associated with sea ice loss. When the moisture flux is broken down into poleward and equatorward components, we see an increase in both poleward and equatorward moisture flux across 70° N. The increase in equatorward moisture flux is greater than the increase in poleward moisture flux, particularly in the boreal cold season (SONDJF). A decomposition of the meridional moisture transport reveals that the changes in moisture flux are largely explained by processes occurring on transient time scales and changes in the zonally asymmetric background circulation. Spatially, the largest increases in equatorward moisture fluxes occur in the North Pacific, with over 50% of the increase in global equatorward moisture transport in SONDJF occurring over the North Pacific (120°–240° E). We conclude that this increase in North Pacific equatorward moisture flux can be explained, at least in part, by an increase in frequency and shift in the location of cyclonic Rossby wave breaking near 55°–60° N, although we note that changes in cyclonic Rossby wave breaking events may not capture all of the changes in the transient circulation. Large-scale circulation responses in the zonal winds, cyclonic wind shear, and 500 hPa geopotential heights support this conclusion. Rossby wave breaking has been linked to changes in moisture fluxes in the Gulf of Alaska and North American West Coast regions in prior work, suggesting that large-scale atmospheric dynamics can play an important role in moisture transport in the polar and sub-polar regions (e.g. Ryoo et al. 2013; Payne and Magnusdottir 2014; Baggett et al. 2016; Mundhenk et al. 2016).

We note that these conclusions are drawn based on considering sea ice loss only. In reality, the climate system is more complex and overall changes in midlatitude-Arctic circulation and moisture fluxes are potentially more complicated than what we propose here. Greenhouse gas forcings are often associated with circulation anomalies that oppose those associated with Arctic warming and sea ice loss, and these effects are not necessarily linear (e.g., Butler et al. 2010; McGraw and Barnes 2016; Sun et al. 2015; McKenna et al. 2018). Recently, however, the circulation responses to greenhouse gas warming and sea ice loss have been shown to be more separable than previously thought (e.g. McCusker et al. 2017). For example, Fig. 9 suggests a strengthening of the Aleutian low in response to sea ice loss. This strengthening of the Aleutian low has been previously identified in climate model studies as both a response to greenhouse gas warming (e.g. Gan et al. 2017; McCusker et al. 2017) and to Arctic warming and sea ice loss (e.g. Sun et al. 2015;

Blackport and Kushner 2017). Furthermore, the atmospheric responses to greenhouse gas forcing and sea ice loss may in fact be especially additive in the North Pacific (e.g. Oudar et al. 2017; McCusker et al. 2017). Thus, the overall response of moisture transport over the North Pacific to sea ice loss may in fact offer insights into the broader response when considering the full impacts of climate change.

Finally, we note that this hypothesis does not argue that all increases in Arctic moisture fluxes are an artifact of circulation changes. Nor does it claim that these changes in moisture fluxes associated with cyclonic Rossby wave breaking can explain all of the increases in equatorward IVT associated with transient moisture fluxes. Rather, we simply argue that increases in equatorward moisture transport are associated with circulation changes driven by sea ice loss. Figures 7, 8 and 9 illustrate the importance of the changes in the synoptic-scale, transient circulation by showing that the increase in cyclonic Rossby wave breaking events associated with sea ice loss is accompanied by an increase in equatorward IVT following the peak of the events. Thus, changes in the circulation are important for future Arctic moisture transport and must be considered.

References

Ayarzagüena B, Screen J (2016) Future Arctic sea ice loss reduces severity of cold air outbreaks in midlatitudes. Geophys Res Lett 43:2801–2809

Baggett C, Lee S (2017) An identification of the mechanisms that lead to Arctic warming during planetary-scale and synoptic-scale wave life cycles. J Atmos Sci 74(6):1859–1877

Baggett C, Lee S, Feldstein S (2016) An investigation of the presence of atmospheric rivers over the North Pacific during planetary-scale wave life cycles and their role in Arctic warming. J Atmos Sci 73(11):4329–4347

Barnes EA (2013) Revisiting the evidence linking Arctic amplification to extreme weather in midlatitudes. Geophys Res Lett. https://doi.org/10.1002/grl.50880

Barnes EA, Hartmann DL (2012) Detection of Rossby wave breaking and its response to shifts of the midlatitude jet with climate change. J Geophys Res Atmos 117:D09,117. https://doi.org/10.1002/2012JD017469

Barnes EA, Screen JA (2015) The impact of Arctic warming on the midlatitude jet-stream: can it? Has it? Will it? WIREs Clim Change 6:277–286. https://doi.org/10.1002/wcc.337

Blackport R, Kushner PJ (2017) Isolating the atmospheric circulation response to Arctic sea ice loss in the coupled climate system. J Clim 30:2163–2185

Blackport R, Screen J (2019) Influence of Arctic sea ice loss in autumn compared to that in winter on the atmospheric circulation. Geophys Res Lett 46:2018GL081,469

Burt MA, Randall DA, Branson MD (2016) Dark warming. J Clim 29(2):705–719

Butler AH, Thompson DWJ, Heikes R (2010) The steady-state atmospheric circulation response to climate change-like thermal forcings in a simple general circulation model. J Clim 23:3474–3496. https://doi.org/10.1175/2010JCLI3228.1

Cattiaux J, Peings Y, Saint-Martin D, Trou-Kechout N, Vavrus SJ (2016) Sinuosity of mid-latitude atmospheric flow in a warming world. Geophys Res Lett. https://doi.org/10.1002/2016GL070309

Cohen J, Screen JA, Furtado JC, Barlow M, Whittleston D, Coumou D, Francis J, Dethloff K, Entekhabi D, Overland J, Jones J (2014) Recent Arctic amplification and extreme midlatitude weather. Nat Geosci 7:627–637. https://doi.org/10.1038/ngeo2234

Collins M, Knutti R, Arblaster J, Dufresne JL, Fichefet T, Friedlingstein P, Gao X, Gutowski W, Johns T, Krinner G, Shongwe M, Tebaldi C, Weaver A, Wehner M (2013) Long-term climate change: projections, commitments and irreversibility. In: Climate change 2013: the physical science basis. Contribution of working group I to the fifth assessment report of the intergovernmental panel on climate change

Deser C, Terray L, Phillips AS (2016) Forced and internal compoments of winter air temperature trends over North America during the past 50 years: mechanisms and implications. J Clim 29:2237–2258. https://doi.org/10.1175/JCLI-D-15-0304.1

Deser C, Tomas RA, Alexander M, Lawrence D (2010) The seasonal atmospheric response to projected Arctic sea ice loss in the late twenty-first century. J Clim 23:333–351. https://doi.org/10.1175/2009JCLI3053.1

Dufour A, Zolina O, Gulev S (2016) Atmospheric moisture transport to the Arctic: assessment of reanalyses and analysis of transport components. J Clim 29:5061–5081

Feldstein SB, Lee S (2014) Intraseasonal and interdecadal jet shifts in the Northern Hemisphere: the role of warm pool tropical convection and sea ice. J Clim 27(17):6497–6518

Francis JA, Hunter E (2006) New insight into the disappearing Arctic sea ice. EOS Trans Am Geophys Union 87:509–511. https://doi.org/10.1029/2006EO460001

Francis JA, Vavrus SJ (2015) Evidence for a wavier jet stream in response to rapid Arctic warming. Environ Res Lett. https://doi.org/10.1088/1748-8326/10/1/014005

Franzke C, Woollings T, Martius O (2011) Persistent circulation regimes and preferred regime transitions in the North Atlantic. J Atmos Sci 68:2809–2825

Franzke CLE, Lee S, Feldstein SB (2016) Evaluating Arctic warming mechanisms in CMIP5 models. Clim Dyn. https://doi.org/10.1107/s00382-016-3263-9

Gan B, Wu L, Jia F, Li S, Cai W, Nakamura H, Alexander MJ, Miller AJ (2017) On the response of the Aleutian low to greenhouse gas warming. J Clim 30:3907–3925

Ghatak D, Miller J (2013) Implications for Arctic amplification of changes in the strength of the water vapor feedback. Geophys Res Lett 118:7569–7578. https://doi.org/10.1002/jgrd.50578

Goss MS, Feldstein SB, Lee S (2016) Stationary wave interference and its relation to tropical convection and Arctic warming. J Clim 29:1369–1389. https://doi.org/10.1175/JCLI-D-15-0267.1

Graversen RG (2006) Do changes in the midlatitude circulation have any impact on the Arctic surface air temperature trend? J Clim 19:5422–5438

Graversen RG, Burtu M (2016) Arctic amplification enhanced by latent energy transport of atmospheric planetary waves. Q J R Meteorol Soc 142:2046–2054. https://doi.org/10.1002/qj.2802

Hansen J, Lacis A, Rind D, Russell G, Stone P, Fung I, Ruedy R, Lerner J (1984) Climate sensitivity: analysis of feedback mechanisms. American Geophysical Union. AGU geophysical monographs, no. 29, Maurice Ewing vol 5

Held IM, Soden BJ (2006) Robust responses of the hydrological cycle to global warming. J Clim 19:5686–5699

Holland MM, Bitz CM (2003) Polar amplification of climate change in coupled models. Clim Dyn 21:221–232. https://doi.org/10.1007/s00382-003-0332-6

Kapsch ML, Graversen RG, Tjernstroöm M, Bintanja R (2016) The effect of downwelling longwave and shortwave radiation on Arctic summer sea ice. J Clim 29:1143–1158. https://doi.org/10.1175/JCLI-D-15-0238.1

Kim BM, Son SW, Min SK, Jeong JH, Kim SJ, Zhang X, Shim T, Yoon JH (2014) Weakening of the stratospheric polar vortex by Arctic sea-ice loss. Nat Commun 5:4646

Kretschmer M, Coumou D, Donges JF, Runge J (2016) Using causal effect networks to analyze different Arctic drivers of midlatitude winter circulation. J Clim 29:4069–4081

Kug JS, Jeong JH, Jang YS, Kim BM, Folland CK, Min SK, Son SW (2017) Two distinct influences of Arctic warming on cold winters over North America and East Asia. Nat Geosci 8:759–762. https://doi.org/10.1038/ngeo2517

Labe Z, Peings Y, Magnusdottir G (2018) Contributions of ice thickness to the atmospheric response from projected Arctic sea ice loss. Geophys Res Lett 45:2018GL078,158

Lang A, Yang S, Kaas E (2017) Sea ice thickness and recent Arctic warming. Geophys Res Lett 44:2016GL071,274

Langen PL, Alexeev VA (2007) Polar amplification as a preferred response in an idealized aquaplanet GCM. Clim Dyn. https://doi.org/10.1007/s00382-006-0221-x

Lee S (2014) A theory for polar amplification from a general circulation perspective. Asia Pac J Atmos Sci 50:31–43

Liu C, Barnes EA (2015) Extreme moisture transport into the Arctic linked to Rossby wave breaking. J Geophys Res Atmos 120:3774–3788. https://doi.org/10.1002/2014JD022796

Liu C, Ren X, Yang X (2014) Mean flow-storm track relationship and Rossby wave breaking in two types of El-Niño. Adv Atmos Sci 31(1):197

Manabe S, Stouffer RJ (1980) Sensitivity of a global climate model to an increase of CO_2 concentration in the atmosphere. J Geophys Res 85:5529–5554

Manabe S, Wetherald RT (1975) The effects of doubling the CO_2 concentration on the climate of a general circulation model. J Atmos Sci 32(1):3–15

McCusker K, Fyfe J, Sigmond M (2016) Twenty-five winters of unexpected Eurasian cooling unilkely due to Arctic sea-ice loss. Nat Geosci 9:838–842. https://doi.org/10.1038/ngeo2820

McCusker KE, Kushner PJ, Fyfe JC, Sigmond M, Kharin VV, Bitz CM (2017) Remarkable separability of circulation response to Arctic sea ice loss and greenhouse gas forcing. Geophys Res Lett L074327:7955–7964

McGraw MC, Barnes EA (2016) Seasonal sensitivity of the eddy-driven jet to tropospheric heating in an idealized AGCM. J Clim 29:5223–5240. https://doi.org/10.1175/JCLI-D-15-0723.1

McKenna CM, Bracegirdle TJ, Shuckburgh EF, Haynes PH, Joshi MM (2018) Arctic sea ice loss in different regions leads to contrasting Northern Hemisphere impacts. Geophys Res Lett L076433:945–954

Messori G, Woods C, Caballero R (2018) On the drivers of wintertime temperature extremes in the high Arctic. J Clim 31:1597–1618. https://doi.org/10.1175/JCLI-D-17-0386.1

Mortin J, Svensson G, Graversen RG, Kapsch ML, Stroeve JC, Boisvert LN (2016) Melt onset over Arctic sea ice controlled by atmospheric moisture transport. Geophys Res Lett 43(12):6636–6642

Mundhenk BD, Barnes EA, Maloney ED, Nardi KM (2016) Modulation of atmospheric rivers near Alaska and the U.S. West Coast by northeast Pacific height anomalies. J Geophys Res Atmos 121:12,751–12,765. https://doi.org/10.1002/2016JD025350

Newman M, Kiladis GN, Weickmann KM, Ralph FM, Sardeshmukh PD (2012) Relative contributions of synoptic and low-frequency eddies to time-mean atmospheric moisture transport, including the role of atmospheric rivers. J Clim 25:7341–7361. https://doi.org/10.1175/JCLI-D-11-00665.1

Oudar T, Sanchez-Gomez E, Chauvin F, Cattiaux J, Terray L, Cassou C (2017) Respective roles of direct GHG radiative forcing and induced Arctic sea ice loss on the Northern Hemisphere atmospheric circulation. Clim Dyn 49:3693–3713

Overland J, Francis JA, Hall R, Hanna E, Kim SJ, Vihma T (2015) The melting Arctic and midlatitude weather patterns: are they connected? J Clim 28:7917–7932

Park DSR, Lee S, Feldstein SB (2015) Attribution of the recent winter sea ice decline over the Atlantic sector of the Arctic Ocean. J Clim 28:4027–4033. https://doi.org/10.1175/JCLI-D-15-0042.1

Park HS, Lee S, Son SW, Feldstein SB, Kosaka Y (2015) The impact of poleward moisture and sensible heat flux on Arctic winter sea ice variability. J Clim 28:5030–5040. https://doi.org/10.1175/JCLI-D-15-0074.1

Payne AE, Magnusdottir G (2014) Dynamics of landfalling atmospheric rivers in the North Pacific in 30 years of MERRA reanalysis. J Clim 27:7133–7150. https://doi.org/10.1175/JCLI-D-14-00034.1

Peings Y, Cattiaux J, Vavrus S, Magnusdottir G (2017) Late twenty-first-century changes in the midlatitude atmospheric circulation in the CESM large ensemble. J Clim 30:5943–5960. https://doi.org/10.1175/JCLI-D-16-0340.1

Peings Y, Magnusdottir G (2014) Response of the wintertime Northern Hemisphere atmospheric circulation to current and projected Arctic sea ice decline: a numerical study with CAM5. J Clim 27:244–264. https://doi.org/10.1175/JCLI-D-13-00272.1

Peixóto JP, Oort AH (1992) Physics of climate. American Institute of Physics, US. https://www.osti.gov/biblio/7287064

Riviére G (2011) A dynamical interpretation of the poleward shift of the jet streams in global warming scenarios. J Atmos Sci 68:1253–1272

Ronalds B, Barnes E, Hassanzadeh P (2018) A barotropic mechanism for the response of jet stream variability to Arctic amplification and sea ice loss. J Clim 31:7069–7085. https://doi.org/10.1175/JCLI-D-17-0778.1

Ryoo JM, Kaspi Y, Waugh DW, Kiladis GN, Waliser DE, Fetzer EJ, Kim J (2013) Impact of Rossby wave breaking on U.S. West Coast winter precipitation during ENSO events. J Clim 26:6360–6382. https://doi.org/10.1175/JCLI-D-12-00297.1

Screen J (2014) Arctic amplification decreases temperature variance in northern mid-to high-latitudes. Nat Clim Change 4:577–582. https://doi.org/10.1038/nclimate2268

Screen J (2017) Simulated atmospheric response to regional and pan-Arctic sea ice loss. J Clim 30:3945–62

Screen JA, Deser C, Smith DM, Zhang X, Blackport R, Kushner PJ, Oudar T, McCusker KE, Sun L (2018) Consistency and discrepancy in the atmospheric response to Arctic sea-ice loss across climate models. Nat Geosci 11:155–163

Screen JA, Deser C, Sun L (2015) Projected changes in regional climate extremes arising from Arctic sea ice loss. Environ Res Lett. https://doi.org/10.1088/1748-9326/10/8/084006

Screen JA, Francis JA (2016) Contribution of sea-ice loss to Arctic amplification is regulated by Pacific Ocean decadal variability. Nat Clim Change 6:856–860. https://doi.org/10.1038/nclimate3011

Screen JA, Simmonds I (2010) Increasing fall-winter energy loss from the Arctic Ocean and its role in Arctic temperature amplification. Geophys Res Lett 37:L16,707. https://doi.org/10.1029/2010GL044136

Serreze MC, Barrett AP, Stroeve J (2012) Recent changes in tropospheric water vapor over the Arctic as assessed from radiosondes and atmospheric reanalyses. J Geophys Res Atmos. https://doi.org/10.1029/2011JD017421

Serreze MC, Barry RG (2005) The Arctic climate system. Cambridge University Press, Cambridge

Serreze MC, Barry RG (2011) Processes and impacts of Arctic amplification: a research synthesis. Glob Planet Change 77:85–96. https://doi.org/10.1016/j.gloplacha.2011.03.004

Smith DM, Dunstone NJ, Scaife AA, Fiedler EK, Copsey D, Hardiman SC (2017) Atmospheric response to Arctic and Antarctic sea ice: the importance of ocean–atmosphere coupling and the background state. J Clim 30:4547–4565

Sorteberg A, Walsh J (2008) Seasonal cyclone variability at 70 ° N and its impact on moisture transport into the Arctic. Tellus 60A:570–586

Strong C, Magnusdottir G (2008) Tropospheric Rossby wave breaking and the NAO/NAM. J Atmos Sci 65(9):2861–2876

Sun L, Deser C, Tomas RA (2015) Mechanisms of stratospheric and tropospheric circulation response to projected Arctic sea ice loss. J Clim 28:7824–7845. https://doi.org/10.1175/JCLI-D-15-0169.1

Sun L, Perlwitz J, Hoerling M (2016) What caused the recent "Warm Arctic, Cold Continents" trend pattern in winter temperatures? Geophys Res Lett 43:5345–5352. https://doi.org/10.1002/2016GL069024

Sung MK, Kim BM, Baek EH, Lim YK, Kim SJ (2016) Arctic–North Pacific coupled impacts on the late autumn cold in North America. Environ Res Lett 11:084,016

Thorncroft C, Hoskins B, McIntyre M (1993) Two paradigms of baroclinic-wave life-cycle behaviour. Q J R Meteorol Soc 119:17–55

Tyrlis E, Hoskins BJ (2008) The morphology of Northern Hemisphere blocking. J Atmos Sci 65:1653–1665. https://doi.org/10.1175/2007JAS2338.1

Walsh J (2014) Intensified warming of the Arctic: causes and impacts on middle latitudes. Glob Planet Change 117:52–63

Woods C, Caballero R (2016) The role of moist intrusions in winter Arctic warming and sea ice decline. J Clim 29:4473–4485. https://doi.org/10.1175/JCLI-D-15-0773.1

Woods C, Caballero R, Svensson G (2013) Large-scale circulation associated with moisture intrusions into the Arctic during winter. Geophys Res Lett 40:4717–4721. https://doi.org/10.1002/grl.50912

Woollings T, Hannachi A, Hoskins B (2010) Variability of the North Atlantic Eddy-driven jet stream. Q J R Meteorol Soc 136:856–868. https://doi.org/10.1002/qj.625

Wu Y, Smith K (2016) Response of Northern Hemisphere midlatitude circulation to Arctic amplification in a simple atmospheric general circulation model. J Clim 29(6):2041–2058

Zappa G, Pithan F, Shepherd T (2018) Multimodel evidence for an atmospheric circulation response to Arctic sea ice loss in the CMIP5 future projections. Geophys Res Lett 45:L076,096. https://doi.org/10.1002/2017GL076096